Stability and Performance of (Cu/Ag)-Sb-I Rudorffite Thin Films for Photovoltaic Applications

Andreas Weis[a,‡], Rik Hooijer[a,‡], Waldemar Kaiser[b], Alexander Biewald[a], Patrick Dörflinger[c], Clement Maheu[d], Oleksandr Arsatiants[a], David Helminger[a], Vladimir Dyakonov[c], Achim Hartschuh[a], Edoardo Mosconi[b], Filippo De Angelis[b,e,f,g], Thomas Bein[a,*]

[a] *Department of Chemistry and Center for NanoScience (CeNS), University of Munich (LMU), Butenandtstr. 11, 81377 Munich, Germany*

[b] *Computational Laboratory for Hybrid/Organic Photovoltaics (CLHYO), Istituto CNR di Scienze e Tecnologie Chimiche "Giulio Natta" (CNR-SCITEC), 06123 Perugia, Italy*

[c] *Experimental Physics VI, Julius Maximilian University of Würzburg. 97074 Würzburg,*

[d] *Surface Science Laboratory, Department of Materials and Earth Sciences, Technical University of Darmstadt, Otto-Berndt-Strasse 3, 64287 Darmstadt, Germany*

[e] *Department of Chemistry, Biology and Biotechnology, University of Perugia, 06123, Italy*

[f] *Department of Natural Sciences & Mathematics, College of Sciences & Human Studies, Prince Mohammad Bin Fahd University, Al Khobar 31952, Saudi Arabia*

[g] *SKKU Institute of Energy Science and Technology (SIEST) Sungkyunkwan University, Suwon, Korea 440-746.*

‡ These authors contributed equally to this work

*Author for correspondence, bein@lmu.de

Abstract

In the search for lead-free perovskites, silver pnictohalides recently gained attention as novel perovskite-inspired materials for photovoltaics due to their high stability, low toxicity and promising early efficiencies, especially for indoor applications. Recent research on such "rudorffites" mainly addresses silver bismuth iodides (Ag-Bi-I), while their antimony analogs are hardly investigated due to intrinsic challenges in the synthesis of Sb-based thin films. Here, we establish a synthetic route to prepare Ag-Sb-I thin films by employing thiourea as Lewis-base additive. Thin film morphologies were further optimized by alloying with Cu, resulting in improved power conversion efficiencies of 0.7% by reducing undesired side phases. Density functional theory calculations and optical characterization methods support the incorporation of Cu into a $Cu_{1-x}Ag_xSbI_4$ phase, keeping the overall stoichiometry and band gap virtually unchanged upon alloying. Our results further reveal the detrimental role of Ag point defects representing trap states in the band gap, being responsible for low open-circuit voltages and sub-gap absorption and emission features. Moreover, additional minor amounts of Bi are shown to boost efficiency and stabilize the performance over a wider compositional range. Despite the remaining challenges regarding device performance, we demonstrate a strong increase in external quantum efficiency when reducing the light intensity, highlighting the potential of Ag-Sb-I rudorffites for indoor photovoltaics.

Introduction

Lead-halide perovskites have drawn enormous interest for optoelectronics applications, particularly photovoltaics, from industry and research alike. Still, the practical applications of these materials remain limited by their notorious instability coupled with the high toxicity of the constituents and degradation products.[1–3] Nonetheless, through the recent upsurge of emerging semiconducting materials, the focus of photovoltaic research has greatly shifted from purely inorganic materials such as silicon or CIGS with high energy demands for production to novel compounds that combine favorable optoelectronic properties with remarkable defect tolerance, in combination with low-temperature solution syntheses.[4–8]

Starting from the prototypical methylammonium lead iodide, $MAPbI_3$, a classical strategy to circumvent the toxicity issues is homovalent or heterovalent substitution of the central lead atom while retaining the perovskite structure. This is commonly achieved through elements with the same ns^2 electronic configuration, as this was repeatedly suggested to be the basis of the exceptional defect tolerance in lead-halide perovskites.[9–11] An obvious and intensely studied candidate for substitution is the group IV neighbor tin, which was shown to be both efficient and less problematic than lead in terms of environmental impact.[12,13] Nonetheless, $MASnI_3$ and other Sn(II) based compounds are highly sensitive towards oxidation, requiring pure precursor chemicals and non-oxidizing solvents, which still hampers the successful implementation of these materials. [14–17] Alternative approaches combine adjacent elements of tin and lead in the periodic table, namely trivalent antimony(III) and bismuth(III), which still showcase the characteristic electronic ns^2 configuration, with monovalent cations like silver and copper, as prominently seen and studied in the archetype double-perovskite $Cs_2AgBiBr_6$.[18,19] Although this compound exhibits several promising properties like long charge carrier lifetime and high environmental stability, the photovoltaic efficiency is limited by rapid non-radiative recombination and a large bandgap.[18–20]

If the monovalent metal ion is omitted entirely in the above systems, the original perovskite structure is sacrificed, leading to another class of perovskite-derived materials with the general structural formula $A_3B_2X_9$, which also suffer from detrimental factors such as high exciton binding energies, strong exciton-phonon coupling and low dimensionality, among others.[21–24] Herein, the A-site cations are mostly derived from the lead-based perovskite counterparts, namely methylammonium, formamidinium or cesium(I). Many reports have already shown the significant influence of this cation, not only on the electronic properties but also as structure directing agent.[25,26]

Most recently, a new class of (Sb/Bi)-based materials has emerged, with the accompanying monovalent A cations being silver and/or copper, featuring the general structural formula $A_xB_yX_{x+3y}$ and straying even further away from the original perovskite lattice. These compounds were coined "rudorffites"[27] in previous reports and are comprised of interconnected $[A/B]X_6$ octahedra, where the A and B cations share equivalent lattice positions, thereby inducing a high degree of stoichiometric freedom. Notably, these pnictohalides show favorable bandgaps for single-junction solar cell devices and high absorption coefficients.[27,28] The hitherto published materials are mostly based on Ag-Bi-I and were shown to already surpass 5 % PCE within only a couple of years' time.[29] Moreover, rudorffites were also employed successfully in other types of devices like X-ray detectors[30], memristors[31] or, as of latest, as highly efficient indoor light harvesters,[32,33] competing with commercial solar cells in this field. Alloying and substituting Ag with Cu was also shown to be an efficient way to tailor their structural and electronic properties.[32,33]

While research efforts to date have been mostly focused on Bi-based rudorffite structures, only few reports concerning pure (Ag/Cu)-Sb-I materials can be found, some of which being inconclusive about important properties like color, bandgap and structure.[34,35] This may be due to synthetic difficulties when working with SbI_3 as precursor[36], which exhibits a high vapor pressure and is prone to evaporation when using film annealing temperatures above 100 °C. Furthermore, instability of the pristine $AgSbI_4$ under ambient conditions was reported as well.[37]

Herein, we demonstrate the thin-film synthesis of $Cu_xAg_{1-x}SbI_4$ (CASI) rudorffites using a Lewis-base assisted approach. We establish the formation of the crystalline target materials in thin films and furthermore we highlight the beneficial effect of an optimal ratio of 40% Cu to Ag on the morphology, reducing grain boundaries and improving the overall coverage. Notably, an additional incorporation of only 5% Bi led to the aforementioned morphology improvement over a broader range up to a Cu content of 90%, which can also be seen in the photovoltaic performance. Density functional theory (DFT) calculations investigate the impact of the stoichiometry of various (Cu/Ag)-Sb-I phases, highlighting the incorporation of Cu into the layered $Cu_xAg_{1-x}SbI_4$ composition. Ultraviolet photoelectron spectroscopy measurements demonstrate the disappearance upon Cu addition of other trivalent oxide antimony states like SbO_x and SbI_3 as side phases likely created through degradation and surface oxidation. UV-Vis spectroscopy and photoluminescence measurements further reveal the presence of deep defect states and broad emission with large Stokes shift, confirmed by DFT calculations, pointing to extraordinarily low Ag point defect formation energies of 0.16 eV. Additionally, PL measurements reveal static emission and lifetime characteristics over the whole doping range,

which we discuss in view of varying charge carrier mobilities and photovoltaic performance. Conceptually, we connect the luminescence behavior to the thin film morphology via hyperspectral optical measurements, explaining the improved performance in solar cells when using an optimal copper content. Lastly, EQE measurements reveal a much-improved photocurrent at low photon flux when no white light bias is employed, hinting at great promise of these materials for indoor photovoltaic applications.

Results and Discussion

To synthesize thin films based on CASI, a common spin-coating approach was employed by dissolving the corresponding halide precursors (CuI/AgI/SbI_3) in a mixture of 1:1 DMF:DMSO to achieve a concentration of approximately 0.6 M, followed by deposition on different substrates (glass/FTO/ITO/mp-TiO_2). Furthermore, a small amount of the Lewis base thiourea (TU) was added to retard the crystallization of the thin film, a crucial step in controlling the formation of the CASI material, which has been reported to exhibit significant stability issues.[37,39,40] This is a necessary step to obtain working devices and circumvent recurrent problems of the halide precursors, with AgI being only hardly soluble in organic solvents like DMF that are commonly used for spin-coating. The influence of the additive on the behavior of the precursor solution is presented in **Figure S1** in the Supporting Information (SI). Similar effects have been shown for lead-based and lead-free perovskites.[41–44] Furthermore, SbI_3 is known to have a high equilibrium vapor pressure[36] which prohibits the use of elevated annealing temperatures, shown to be crucial for the formation of the Bi analogue.[45] In this work, we therefore employed a ramped thermal annealing approach from 50 °C for 1 h to 80 °C for a minute to anneal the films. An 'inverse' technique based on one short immediate heating step for 1 min at 120 °C leads to improved crystallinity but less complete coverage, as shown in the XRD graphs and SEM images in **Figure S3**.

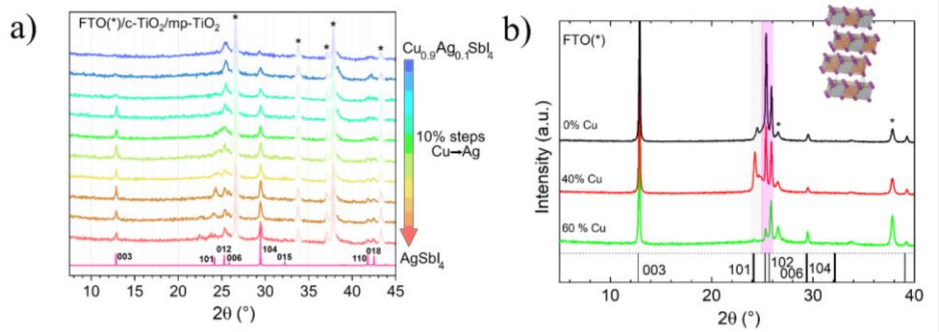

Figure 1: Thin film XRD data normalized to the highest intensity on FTO/c-TiO_2/mp-TiO_2 (a) and on FTO (b) of $Cu_xAg_{1-x}SbI_3$ thin films. a) Increasing Cu concentrations in steps of 10% coded from red to blue with theoretical patterns from Oldag et al.[38] The FTO reflections are removed for correct normalization and marked by an asterisk (*). b) $Cu_xAg_{1-x}SbI_3$ films on FTO with 0%, 40% and 60% Cu with [101] reflections highlighted in light gray and the [102]/[006] peak in light pink. Inset: Crystal structure used for simulation of $AgSbI_4$. c-TiO_2 refers to compact TiO_2 and mp-TiO_2 to mesoporous.

The XRD patterns for $Cu_xAg_{1-x}SbI_3$ films on FTO/c-TiO_2/mp-TiO2 are shown in Figure 1a for incremental replacement of Ag with Cu in 10% steps. The substrate material was chosen to reflect the crystallization conditions which will be later adopted in solar cell devices.

The patterns were normalized after removing the additional reflections arising from the substrate. As these match very well with the theoretical patterns extracted from the Bi analogue $AgBiI_4$,[46] we assume a similar space group (R3m) and a related crystal structure based on the $CdCl_2$ prototype (Figure 1b), in line with Gray et al.[40] Materials based on $A_xB_yX_{x+3y}$ stoichiometries with A being a monovalent transition metal cation (Ag^+/Cu^+), B a trivalent pnictogen cation (Bi^{3+}/Sb^{3+}) and X a monovalent halide anion, commonly I^-, are constructed of alternating occupied and unoccupied positions of edge-sharing octahedra $[AX_6]^{5-}$, $[BX_6]^{3-}$ and $[\Delta X_6]^{6-}$ (Δ = vacancy).[39] In our case, the halide ions occupy the octahedral corners (Wyckoff *6c*) and Ag/Cu/Sb occupy the Wyckoff positions *3a* in the octahedral center.[46] Nonetheless, because of the aforementioned disorder, exact crystal structure analysis of such materials was shown to be a challenge.[39,47] This is caused by an important feature in rudorffites, namely A and B cations occupying the same Wyckoff sites, which enables a vast number of compositional permutations. In recent years, different elemental compositions for Ag-Bi-I systems were explored experimentally, ranging from $AgBi_2I_7$ to Ag_3BiI_6.[27,48–50] Furthermore, for silver- or copper-rich compositions, the monovalent A cations additionally may occupy the *3b* positions in-between the octahedral slabs.[39,50] As shown later, we can carefully exclude compositions of other stoichiometries than the $AgSbI_4$ one on the basis of our theoretical calculations, which suggest that a band gap collapse can be observed by having an excess of Ag in comparison to Sb or vice versa, in line with previous considerations on the Bi-based analogues.[47]

Interestingly, the peak positions in Figure 1a only show a very small shift upon incremental alloying with Cu, suggesting no significant change of the unit cell. The most pronounced change is the intensity decrease of the [104] and [003] reflections for increased Cu content. Furthermore, the intensity ratio of the neighboring [102]/[006] peaks reverses when more Cu is introduced, which can be seen in more detail in Figure 1b for films deposited on FTO despite a strong orientation along the [003] direction. This intensity change is linked to a decrease in sectional symmetry because of additional tetrahedral Cu polytypes centered at the 3a positions of Cu in the layers, as demonstrated by our DFT calculations which will be discussed later.

Previous reports suggested an intrinsic instability of the $AgSbI_4$ phase, whereas the Bi-based analog with a larger ionic radius was shown to be highly stable under synthesis and in ambient conditions.[40] Moreover, Al-Anesi et al. showed local symmetry enhancement through Sb

doping of Cu_2AgBiI_6, thereby improving photovoltaic efficiency through enhanced local structural symmetry and thus reduced defect density.[33] Consequently, we also prepared a system with only a small addition of 5 % Bi, resulting in a decrease in band gap (see below) and improved morphology. The corresponding XRD patterns show no significant change when comparing Bi-alloyed structures versus the pristine antimony thin films (see **Figure S4**).

In the following, we focus on samples with 0%, 40% and 60% Cu:Ag, as they are exemplary for the electronic and morphological changes in this system. The SEM images for those samples, shown in Figure 2a-f, highlight the strong impact of the monovalent halide precursor on morphology and crystallization. First of all, the addition of Bi seems to generally aid the crystallization, resulting in films with significantly better coverage and homogeneous morphologies. Enhanced lattice stability may further rationalize the increased coverage and high homogeneity at 40 % Cu, resulting in overall homogeneously covered films. Beyond 50 % Cu, the homogeneity decreases again.

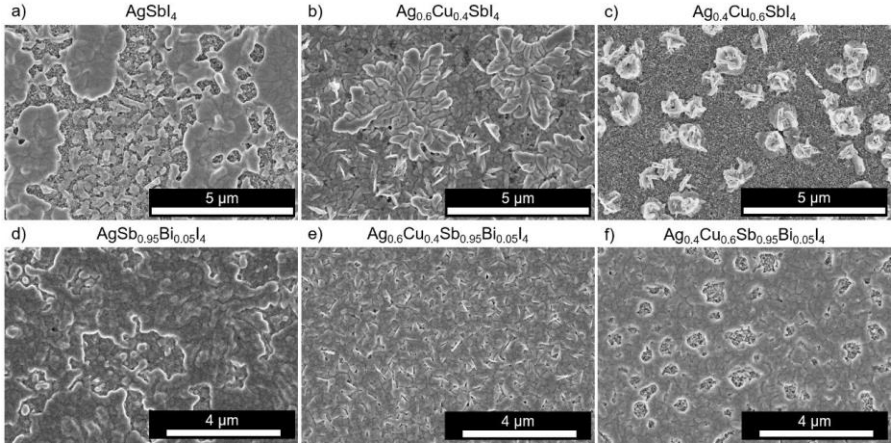

Figure 2: Scanning electron microscopy images of $Cu_xAg_{1-x}SbI_4$ thin films on FTO/c-TiO_2/mp-TiO_2. a)-c) Increasing amount of Cu (0%, 40%, 60%) and d)-f) increasing amount of Cu (0%, 40%, 60%) combined with 5% Bi/Sb substitution.

XPS spectra confirm the incorporation of Cu and the presence of the expected elements, verifying the formation of the pure silver and copper-alloyed phases, see SI **Figure S2a-c**. Interestingly, the XPS spectra of the pure $AgSbI_4$, shown in SI **Figure S2c,** show additional states of either SbO_x, which could result from surface oxidation, or SbI_x side phases at approximately 585.5 eV. These side phases vanish when Cu is added to the system (see SI **Figure S2**).

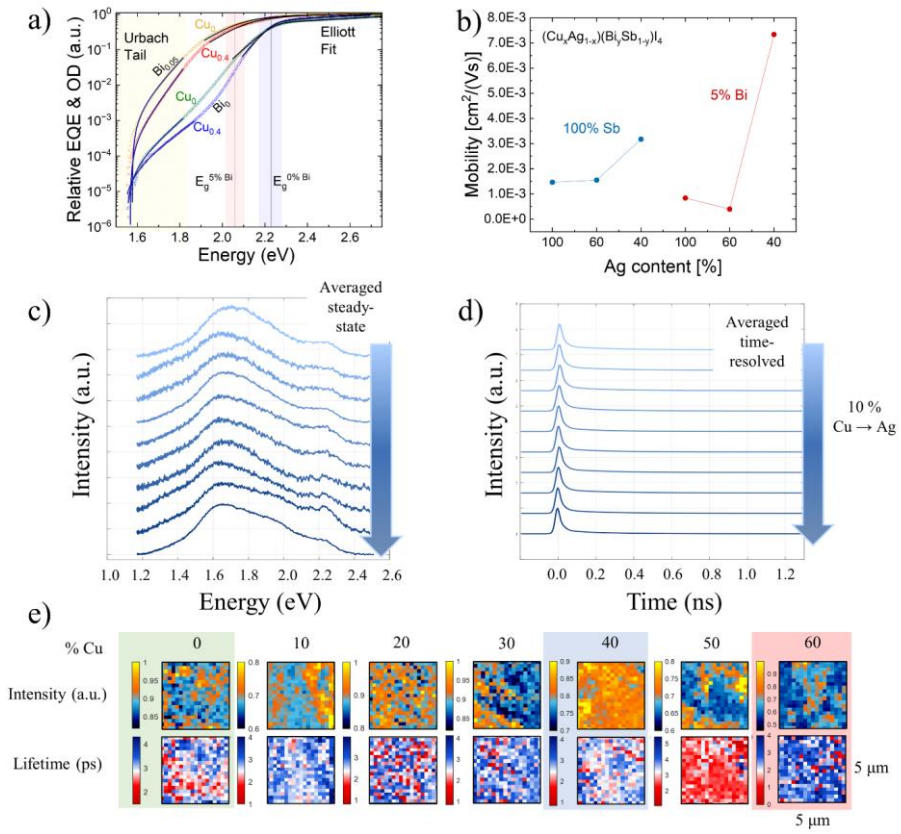

Figure 3: a) Fitted absorption coefficient of $AgSbI_4$ (green), $Cu_{0.4}Ag_{0.6}SbI_4$ (blue), $AgBi_{0.05}Sb_{0.95}I_4$ (yellow), $Cu_{0.4}Ag_{0.6}Bi_{0.05}Sb_{0.95}I_4$ (red). The red and blue boxes highlight the bandgap extracted from the Elliott fits. The straight lines around the band edge are fitted with Elliott's method and the black lines in the bandgap are exponential Urbach tails. b) Mobility values extracted from TRMC measurements for Ag concentrations of 100%, 60%, 40% without (blue) and with 5% Bi substitution (red). c) Averaged spectra from photoluminescence measurements for incremental Cu percentage from 0% to 100% without Bi addition (dark to light blue: increasing Cu content). The yellow box highlights the self-trapped exciton emission and the light blue box the band-to-band emission. d) Averaged time-resolved photoluminescence measurements for incremental Cu percentage from 0% to 100% without Bi addition. (dark to light blue: increasing Cu content) e) Hyperspectral images of the photoluminescence intensity and time-resolved photoluminescence intensity distribution on a 5 µm x 5 µm large area of a $Cu_xAg_{1-x}SbI_4$ thin film with composition ranging from 0% to 60% Cu/Ag ratio. The pixel size is 35x35.

We now employ a combined fitting procedure following Elliott's method for the absorption coefficient close to the band edge and Urbach's tail to quantify the bandgap and sub-bandgap states.[51] The band gap of $AgSbI_4$ lies within the range of 2.0 - 2.2 eV, as in Figure 3a for $AgSbI_4$ (green), $Cu_{0.4}Ag_{0.6}SbI_4$ (blue), $Bi_{0.05}$:$AgSbI_4$ (orange), $Bi_{0.05}$:$Cu_{0.4}Ag_{0.6}SbI_4$ (red). Changing the Cu:Ag ratio does not significantly alter the band gap, while the addition of Bi reduces the bandgap by 0.2 eV. The decrease in band gap upon Bi/Sb alloying has previously been successfully assigned to the formation of aggregates rich of either Sb or Bi for similar materials, being the source of the reduction in the electronic band gap.[52] [24] Furthermore, the Urbach tails all converge to the same energy of around 1.6 eV, pointing to the presence of trap states. This deep contribution is reduced through incorporation of 40 % Cu, which is most likely tied to the improved crystallinity and morphology, suggesting that fewer defects are introduced in the synthesis compared to the reference systems as confirmed by absorbance log plots (**SI Figure S6**). These disorder-related deep levels are also confirmed by the photoluminescence emission as seen in Figure 3c, where the main emission maximum lies at around 1.6 eV as well, with only a small contribution at the band edge (2.3 eV), which agrees well with the band gap obtained from the Elliot fits. This low energy emission is probably caused by self-trapped excitons and defects dominating the emission behavior, which was reported to be induced by exciton-phonon coupling and the resulting ultrafast carrier localization in multiple lead-free perovskite materials.[53–55] Furthermore, the lifetimes are also unaffected by additional Cu doping, and occur in the range of only ps (Figure 3d). The detailed spectral trends of photoluminescence and lifetime measurements for all samples are shown in **Figure S8**, with only negligible intensity and lifetime differences evident.

Mobility values for the thin films, extracted from TRMC, highlight an overall increase when reducing the silver contribution, shown in Figure 3b. This is in line with previous reports on the related $Cu_{4x}(AgBi)_{1-x}I_4$ compound, where small polaron formation was found to be responsible for ultrafast charge carrier localization that could be mitigated via the introduction of Cu.[53,54] The mobility values are mostly low when compared to other double perovskites like $Cs_2AgBiBr_6$.[56] Moreover, Bi addition does not increase the overall mobility in the pure $AgSbI_4$, but significantly boosts the mobility for systems with Cu in excess of 60%.

To connect the optical properties with the morphology changes upon Cu doping, we performed FLIM measurements; results are shown in Figure 3e. Here, the intensity of the PL emission and the lifetime are spectrally and spatially resolved on a film area of the size 5 μm x 5 μm. These

results confirm the trend of increased homogeneity of the surface of film samples alloyed with 40 % Cu, showing the most consistent lifetimes overall and the best (homogeneous) distribution of luminescence intensity. The latter decreases sharply at 50 % Cu and above, drastically decreasing the lifetime of the whole sample area. Keeping in mind the similar electronic characteristics over the whole substitution range, these measurements reveal the important role of the A cation in such structures, directing morphology, excitation behavior over a bigger sample size and, as shown in Figure 5, device performance and statistics.

DFT calculations were then performed to shed light on the impact of composition of the Ag-Sb-I and Cu/Ag-Sb-I rudorffite phases. Ionic positions and cell parameters were optimized on the PBE level of theory including D3 dispersion corrections, with refined PBE0+SOC calculations for formation energies and electronic band gaps; see computational details in the SI. The cubic $ThZr_2H_7$-type $AgSb_2I_7$ stoichiometry[47,57–59], see **Figure S9**, is unlikely to form as seen in the large formation energies of 4.86 eV/f.u., see Table 1. Additionally, predicted band gaps of 0.39 eV, far below the experimental values, rule out the existence of $AgSb_2I_7$ stoichiometry, in line with studies on its Bi-based counterpart.[47] $AgSbI_4$ and Ag_3SbI_6 phases show disorder in their position of Sb and Ag ions, see **Figures S10** and **S11**. Starting from the structure of the Bi-based counterparts,[38,57,60] a configurational screening was performed to obtain low energy configurations using DFT. Both compositions ($AgSbI_4$ and Ag_3SbI_6) show low energy structures with formation energies of -0.01 eV and 0.03 eV with band gaps of 2.07 and 1.78 eV for $AgSbI_4$ and Ag_3SbI_6, respectively. Recalling the experimental bandgap values of ~2.0 – 2.2 eV, this supports the existence of layered $AgSbI_4$ phases, see Figure 4a, while Ag_3SbI_6-rich side phases may contribute to the sub-gap absorption and emission features. The DOS of the $AgSbI_4$ phase shows the expected dominant role of iodide at the valence band edge, while the conduction band edge is dominated by Sb and I states from the SbI_6 octahedra, with limited contribution from Ag, see Figure 4b. Note that entropic contributions, neglected in our study, likely contribute to the phase stabilization of such disordered phases.

Table 1: Optimized lattice parameters (PBE, D3) of the low energy configurations of the Ag-Sb-I and the Cu/Ag-Sb-I rudorffite phases. Formation energies per formula unit and electronic band gaps are given at the PBE0 level of theory with inclusion of SOC corrections on the PBE+D3 optimized geometries. **Table S2** summarizes a configurational analysis for each composition.

System	Formation Energy (eV/f.u.)	Band Gap (eV)	Lattice constants (Å)	Cell Angles (°)
$AgSb_2I_7$	4.86	0.39	a=b=c=14.637	α=β=γ=90

$AgSbI_4$	-0.01	2.07	a = 8.671 b = 8.665 c = 20.804	α=88.97 β=91.11 γ=120.58
Ag_3SbI_6	0.03	1.78	a = 9.178 b = 8.751 c = 20.763	α=86.57 β=92.47 γ=122.65
Cu_2AgSbI_6	0.42	1.90	a = 8.551 b = 8.525 c = 21.452	α=89.96 β=90.11 γ=119.52
$Cu_{0.5}Ag_{0.5}SbI_4$	0.14	2.13	a = 8.671 b = 8.665 c = 20.804	α=88.97 β=91.11 γ=120.58

Moving to the (Cu/Ag)-Sb-I compositions, especially the Cu_2AgSbI_6 phase has recently been proposed to form in the Bi-counterparts.[61] The structure of the given phase is highly disordered, with many cations occupying same lattice positions, requiring a configurational screening, see **Figure S12**. The proposed low energy structure shows a formation energy of 0.42 eV/f.u., containing layers of Ag/Cu-I without Sb incorporated, see configuration c11 in **Figure S12**, which is substantially lower than fully mixed structures, see **Table S2**. This may point to favorable phase segregation in such compounds. Electronic band gap values of 1.90 eV are in fair agreement with experiments. Still, the successful incorporation of Cu ions over a wide range of Cu:Ag alloying in our experimental investigation raises concerns about the relevance of the Cu_2AgSbI_6 phase. Thus, we performed DFT calculations on the $Cu_{0.5}Ag_{0.5}SbI_4$ composition, keeping the overall A-B-X stoichiometry of 1-1-4 and replacing half of the Ag ions by Cu, as suggested by our XRD data in Figure 1. Interestingly, the formation energy of the $Cu_{0.5}Ag_{0.5}SbI_4$ phase, see Figure 4b, decreases to 0.14 eV/f.u. with a band gap of 2.13 eV, in excellent agreement to our experimental thin films. We further predict an upshift of the valence band edge by 0.24 eV compared to the $AgSbI_4$ phase, see Figure 4c. Notably, valence band (VB) XPS spectra (**SI Figure S2d**) show an increase in the VB energy upon Cu addition by ~0.15-0.25 eV, which confirms our DFT results and, most importantly, supports the existence of the 1:1:4 stoichiometry in our synthesized thin films. Thus, we can expect that the 1:1:4 stoichiometry is accessible over a large range of Cu:Ag alloying.

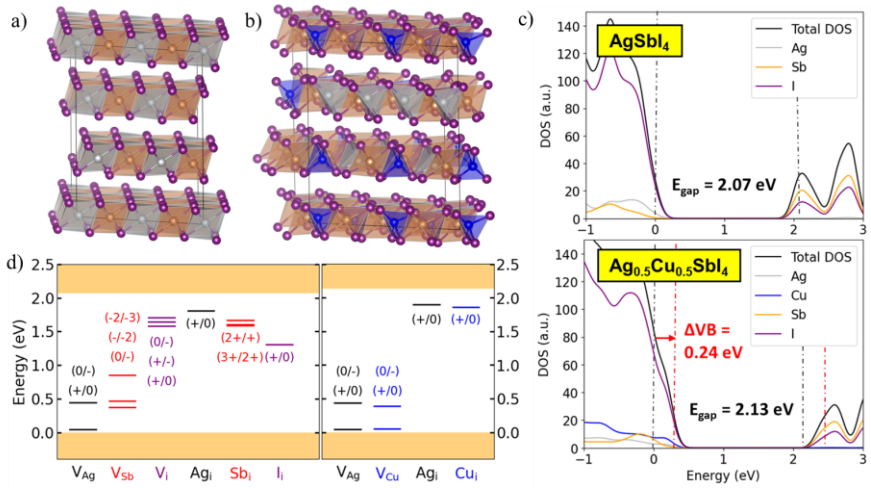

Figure 4: (a, b) Structural representation of $AgSbI_4$ and $Cu_{0.5}Ag_{0.5}SbI_4$, respectively, with following color code: Ag = silver, Cu = blue, Sb = orange, I = purple. (c) Density of states on the PBE0+SOC level of theory of (top) $AgSbI_4$ and (bottom) $Cu_{0.5}Ag_{0.5}SbI_4$. Electronic band gap values are given in each panel. The potential of the considered systems has been aligned with respect to the vacuum level to obtain the VB shift between $AgSbI_4$ and $Cu_{0.5}Ag_{0.5}SbI_4$, as highlighted in red color. The VB maximum of the $AgSbI_4$ phase has been set to zero energy. (d) Thermodynamic ionization levels of point defects, vacancies V_X and interstitials X_i for each element X = (Ag, Cu, Sb, I), based on hybrid PBE0+D3 DFT calculations with inclusion of SOC. The orange colored parts highlight the valence band (bottom) and conduction band (top). Computational details on the defect calculations are provided in the SI.

We further calculate the defect formation energies, see Figure S-C5 to S-C7, and thermodynamic ionization levels (TILs), see Figure 4d, for the pure $AgSbI_4$ and the alloyed $Cu_{0.5}Ag_{0.5}SbI_4$ compounds, respectively. All geometries were optimized on the PBE+D3 level of theory, with refined calculations for DFE and TILs based on the PBE0 level of theory with inclusion of spin-orbit coupling corrections. We observe low DFEs of 0.16 eV for Ag vacancies (V_{Ag}^-) and interstitials (Ag_i^+), representing hole and electron trap states at 0.44 eV above the VBM and 0.25 eV below the CBM, see Figure 4d and **Figure S14**. This suggests that sub-gap emission features at 1.6 eV may likely be caused by recombination of electrons trapped at Ag vacancies. The low formation energies of Ag point defects further are in line with features of Ag-Bi-I compounds that previously have been considered for ionic conduction due to their

mobile Ag ions.[38] Notably, Sb and I point defects also act as trap states within the band gap, see Figure 4d, while showing moderate formation energies of ~0.7 to 0.9 eV, thus being of less relevance for the optoelectronic properties of $AgSbI_4$. Moving towards the alloyed $Cu_{0.5}Ag_{0.5}SbI_4$, we observe negligible differences in the TILs and DFEs (**Figure S15**) for Ag and Cu vacancies and interstitials, in line with the low dependence of sub-gap emission on Cu:Ag alloying as shown in Figure 4c. This suggests further that the reduction of sub-gap absorption upon Cu addition is due to the growth of more homogeneous morphologies rather than a suppression of point defect formation. Consequently, Cu alloying is mainly relevant for reducing AgI rich side phases, while the concentration incremental Cu alloying shifts the type of detrimental defects between Ag and Cu.

After elaborating the structural and electronic properties of the CASI rudorffites, photovoltaic devices were fabricated in the n-i-p architecture with increasing amounts of Cu. Mesoporous titania was used as electron transporting layer and PTAA as hole transporting layer.[27,45,62] The statistical analysis of the device performance can be seen in Figure 5a-f. Firstly, the overall performance increases significantly when employing only a small substitution of 5% Bi, attributed to the band gap decrease. Interestingly, this minor incorporation of Bi additionally stabilizes the performance over a wide range of Cu:Ag ratios, while the performance of pristine Sb-based solar cells breaks down at Cu concentrations above 50 %. We attribute this impact of Bi to the improved homogeneity of the morphology as seen in Figure 2f, hinting at a highly beneficial role of BiI_3 in the precursor solution. In the Bi-free series, samples prepared with 40 % Cu are generally the most efficient, showing the overall highest PCE, mostly due to the increased current density. Notably, the low open circuit voltage is the main bottleneck in these systems, as also suggested previously.[28,29] In our studies, only samples with added Bi surpass 0.4 V open circuit voltage in some cases, whereas Cu-alloyed samples show only small improvements. We attribute the low voltage to non-radiative recombination processes mediated by Ag point defects, representing trap states with low formation energies as shown by our DFT calculations, and ultrafast carrier localization.[51,53]

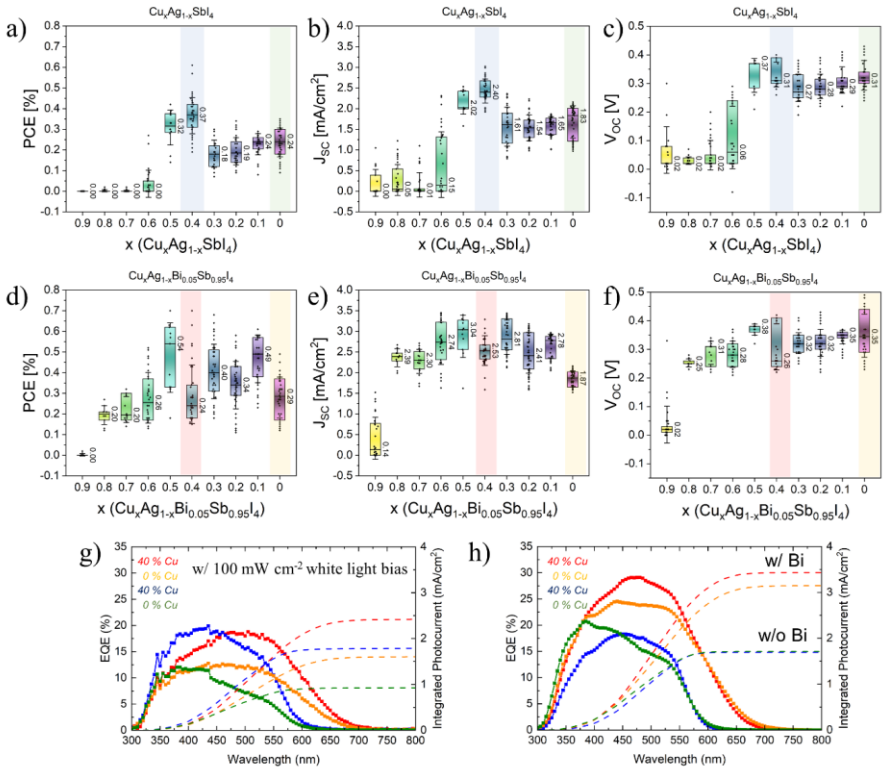

Figure 5: Characterization of photovoltaic devices. a-c) PCE, J_{sc}, V_{oc} statistical box plots with median, interquartile range and statistical outliers for 10% changes of the Cu/Ag ratio from $Cu_{0.9}Ag_{0.1}SbI_4$ to $Cu_{0.0}Ag_{1.0}SbI_4$. The same color scheme for the colored boxes as for Figure 4a was used to highlight the reference and the most efficient alloying step. d-f) PCE, J_{sc}, V_{oc} statistical box plots for 10% changes of Cu/Ag ratio with fixed 5% Bi content from $Cu_{0.9}Ag_{0.1}Bi_{0.05}Sb_{0.95}I_4$ to $Cu_{0.0}Ag_{1.0}$ $Bi_{0.05}Sb_{0.95}I_4$. The same color scheme for the colored boxes as for Figure 4a was used to highlight the reference and the most efficient alloying step. g) and h), EQE spectra and integrated photocurrent density of the most efficient solar cells for $AgSbI_4$ (green), $Cu_{0.4}Ag_{0.6}SbI_4$ (blue), $AgBi_{0.05}Sb_{0.95}I_4$ (orange) and $Cu_{0.4}Ag_{0.6}Bi_{0.05}Sb_{0.95}I_4$ (red). The data in g) were measured with a constant 100 mW/cm^2 white light source in the background, while the data in h) were measured without white light bias.

To further estimate the potential of Sb-based rudorffites for indoor photovoltaics, EQE measurements were carried out on well-performing solar cells with and without white light background illumination. As shown in Figure 5g, the EQE measured under white light illumination at 100 mW/cm^2 is comparably small, with a maximum of 20 % for Cu-alloyed

films at 450 nm without Bi and at 550 nm with Bi. Interestingly, when using a chopped white light source without a white light bias, the overall EQE increases significantly by approximately 10% overall for all thin films except $Cu_{0.4}Ag_{0.6}SbI_4$, which could be explained by a different recombination mechanism at high fluence intensities in this system as seen in the TRMC curves in Figure S7b. This is in line with the behavior of Cu_2AgBiI_6 rudorffites, where the efficiency for indoor light illumination almost doubles up to 10 % iPCE,[33] being attributed to reduced non-geminate recombination, which seems to be an intrinsic feature of (Cu/Ag)-(Sb/Bi)-I based materials.

Although the initial performance falls behind Bi-based "rudorffites"[27,33,58] this class of materials offers great potential for indoor applications while being easily tunable. Furthermore, our results demonstrate the compositional freedom of solution-processed rudorffites. We propose that through stoichiometry tweaking, precursor engineering - i.e. by employing acetates or other metal sources[14,21] - or further additive modification, the performance could be strongly improved to offer a viable alternative for low-cost indoor photovoltaics.

CONCLUSION

To summarize, we successfully synthesized “rudorffite”-type Cu/Ag-Sb-I thin films using the Lewis-base additive thiourea. We establish control of the thin film morphology by partial alloying of Ag with Cu atoms, resulting in homogeneous coverage, which was even improved upon partial substitution with Bi. DFT calculations and optical characterization point to the formation of a $AgSbI_4$ phase in the pure Ag case and the incorporation of Cu ions, partially replacing Ag and forming $Cu_{1-x}Ag_xSbI_4$. Other phases that have been previously discussed for the Bi-based counterparts could be ruled out due to large formation energies or low predicted band gaps. Our results further reveal the detrimental role of Ag point defects, which induce sub-bandgap electronic states that may act as recombination centers resulting in sub gap emission and absorption features. We further demonstrate that Cu alloying does not significantly alter the electronic band gap, which consequently represents a facile strategy for the optimization of Sb-based rudorffites. Solar cells based on the CASI rudorffites show low power conversion efficiencies of around 0.3%, mainly hampered by large losses in the open-circuit voltage. Interestingly, substituting a small amount of 5% bismuth raises the efficiencies to up to 0.7%, mainly through a reduction of the electronic band gap. We observe an apparent stabilization in current density and open-circuit voltage upon addition of Bi over a wide range of Cu:Ag alloys. Finally, white light bias-free EQE measurements suggest a much-improved performance of these materials for indoor photovoltaic applications, which we attribute to reduced geminate recombination at low light intensity. These observations offer opportunities for the control and design of novel Sb-based rudorffites as perovskite-inspired semiconductors with potential for diverse optoelectronic applications such as indoor photovoltaics.

Acknowledgements

The authors acknowledge funding from the Bavarian Network “Solar Technologies Go Hybrid”, the German Science Foundation (DFG) focus program SPP 2196 and the DFG Excellence Cluster e-conversion (EXC 2089/1-390776260). The authors thank Dr. Steffen Schmidt for performing the SEM measurements. W.K, E.M, and F.D.A. acknowledge funding from the European Union’s Horizon Europe research and innovation programme under grant agreement No. 101082176 – VALHALLA and from the European Union- NextGenerationEU under the Italian Ministry of University and Research (MUR) National Innovation Ecosystem grant ECS00000041 - VITALITY. Views and opinions expressed are however those of the author(s) only and do not necessarily reflect those of the European Union or CINEA. Neither the European Union nor the granting authority can be held responsible for them. F.D.A acknowledges Università degli Studi di Perugia and MUR for support within the project Vitality.

Supporting Information

The Supporting Information contains experimental procedures, additional experimental data (UPS, XRD, UV-Vis, JV, PL), computational method (DFT), compositional analysis, further computational results.

References

Commentato [WK1]: Just a comment for changes in the References:

Ref. 14: some authors are missing
Ref. 16+24: Angelis, F. De -> De Angelis, F.

References

(1) Divitini, G.; Cacovich, S.; Matteocci, F.; Cinà, L.; Di Carlo, A.; Ducati, C. In situ observation of heat-induced degradation of perovskite solar cells. *Nat Energy* **2016**, *1* (2), 1–6. DOI: 10.1038/nenergy.2015.12.

(2) Boyd, C. C.; Cheacharoen, R.; Leijtens, T.; McGehee, M. D. Understanding Degradation Mechanisms and Improving Stability of Perovskite Photovoltaics. *Chemical Reviews* **2019**, *119* (5), 3418–3451. DOI: 10.1021/acs.chemrev.8b00336. Published Online: Nov. 16, 2018.

(3) Dunfield, S. P.; Bliss, L.; Zhang, F.; Luther, J. M.; Zhu, K.; Hest, M. F. A. M.; Reese, M. O.; Berry, J. J. From Defects to Degradation: A Mechanistic Understanding of Degradation in Perovskite Solar Cell Devices and Modules. *Adv. Energy Mater.* **2020**, *10* (26), 1904054. DOI: 10.1002/aenm.201904054.

(4) Grätzel, M. The Rise of Highly Efficient and Stable Perovskite Solar Cells. *Accounts of chemical research* **2017**, *50* (3), 487–491. DOI: 10.1021/acs.accounts.6b00492.

(5) Krebs, F. C.; Espinosa, N.; Hösel, M.; Søndergaard, R. R.; Jørgensen, M. 25th anniversary article: Rise to power--OPV-based solar parks. *Advanced Materials* **2014**, *26* (1), 29–38. DOI: 10.1002/adma.201302031.

(6) Li, H.; Zhang, W. Perovskite Tandem Solar Cells: From Fundamentals to Commercial Deployment. *Chemical Reviews* **2020**, *120* (18), 9835–9950. DOI: 10.1021/acs.chemrev.9b00780. Published Online: Aug. 7, 2020.

(7) Kim, G.-W.; Petrozza, A. Defect Tolerance and Intolerance in Metal-Halide Perovskites. *Adv. Energy Mater.* **2020**, *10* (37), 2001959. DOI: 10.1002/aenm.202001959.

(8) Steirer, K. X.; Schulz, P.; Teeter, G.; Stevanovic, V.; Yang, M.; Zhu, K.; Berry, J. J. Defect Tolerance in Methylammonium Lead Triiodide Perovskite. *ACS Energy Lett.* **2016**, *1* (2), 360–366. DOI: 10.1021/acsenergylett.6b00196.

(9) Ganose, A. M.; Savory, C. N.; Scanlon, D. O. Beyond methylammonium lead iodide: prospects for the emergent field of ns2 containing solar absorbers. *Chemical communications (Cambridge, England)* **2016**, *53* (1), 20–44. DOI: 10.1039/C6CC06475B.

(10) Kurchin, R. C.; Gorai, P.; Buonassisi, T.; Stevanović, V. Structural and Chemical Features Giving Rise to Defect Tolerance of Binary Semiconductors. *Chem. Mater.* **2018**, *30* (16), 5583–5592. DOI: 10.1021/acs.chemmater.8b01505.

(11) Brandt, R. E.; Poindexter, J. R.; Gorai, P.; Kurchin, R. C.; Hoye, R. L. Z.; Nienhaus, L.; Wilson, M. W. B.; Polizzotti, J. A.; Sereika, R.; Žaltauskas, R.; Lee, L. C.; MacManus-Driscoll, J. L.; Bawendi, M.; Stevanović, V.; Buonassisi, T. Searching for "Defect-Tolerant" Photovoltaic Materials: Combined Theoretical and Experimental Screening. *Chem. Mater.* **2017**, *29* (11), 4667–4674. DOI: 10.1021/acs.chemmater.6b05496.

(12) Nasti, G.; Abate, A. Tin Halide Perovskite (ASnX 3) Solar Cells: A Comprehensive Guide toward the Highest Power Conversion Efficiency. *Adv. Energy Mater.* **2020**, *10* (13), 1902467. DOI: 10.1002/aenm.201902467.

(13) Serrano-Lujan, L.; Espinosa, N.; Larsen-Olsen, T. T.; Abad, J.; Urbina, A.; Krebs, F. C. Tin- and Lead-Based Perovskite Solar Cells under Scrutiny: An Environmental Perspective. *Adv. Energy Mater.* **2015**, *5* (20), 1501119. DOI: 10.1002/aenm.201501119.
(14) Weis, A.; Ganswindt, P.; Kaiser, W.; Illner, H.; Maheu, C.; Glück, N.; Dörflinger, P.; Armer, M.; Dyakonov, V.; Hofmann, J. P. Heterovalent Tin Alloying in Layered MA3Sb2I9 Thin Films: Assessing the Origin of Enhanced Absorption and Self-Stabilizing Charge States. *J. Phys. Chem. C* **2022**, *126* (49), 21040–21049.
(15) Leijtens, T.; Prasanna, R.; Gold-Parker, A.; Toney, M. F.; McGehee, M. D. Mechanism of Tin Oxidation and Stabilization by Lead Substitution in Tin Halide Perovskites. *ACS Energy Lett.* **2017**, *2* (9), 2159–2165. DOI: 10.1021/acsenergylett.7b00636.
(16) Ricciarelli, D.; Meggiolaro, D.; Ambrosio, F.; Angelis, F. de. Instability of Tin Iodide Perovskites: Bulk p-Doping versus Surface Tin Oxidation. *ACS Energy Lett.* **2020**, *5* (9), 2787–2795. DOI: 10.1021/acsenergylett.0c01174.
(17) Aldamasy, M.; Iqbal, Z.; Li, G.; Pascual, J.; Alharthi, F.; Abate, A.; Li, M. Challenges in tin perovskite solar cells. *Physical chemistry chemical physics : PCCP* **2021**, *23* (41), 23413–23427. DOI: 10.1039/D1CP02596A. Published Online: Oct. 27, 2021.
(18) Tress, W.; Sirtl, M. T. Cs 2 AgBiBr 6 Double Perovskites as Lead-Free Alternatives for Perovskite Solar Cells? *Solar Rrl* **2022**, *6* (2), 2100770. DOI: 10.1002/solr.202100770.
(19) Hoye, R. L. Z.; Eyre, L.; Wei, F.; Brivio, F.; Sadhanala, A.; Sun, S.; Li, W.; Zhang, K. H. L.; MacManus-Driscoll, J. L.; Bristowe, P. D.; Friend, R. H.; Cheetham, A. K.; Deschler, F. Fundamental Carrier Lifetime Exceeding 1 µs in Cs 2 AgBiBr 6 Double Perovskite. *Adv. Mater. Interfaces* **2018**, *5* (15), 1800464. DOI: 10.1002/admi.201800464.
(20) Sirtl, M. T.; Hooijer, R.; Armer, M.; Ebadi, F. G.; Mohammadi, M.; Maheu, C.; Weis, A.; van Gorkom, B. T.; Häringer, S.; Janssen, R. A. J. 2D/3D Hybrid Cs2AgBiBr6 Double Perovskite Solar Cells: Improved Energy Level Alignment for Higher Contact-Selectivity and Large Open Circuit Voltage. *Advanced Energy Materials* **2022**, *12* (7), 2103215.
(21) Giesbrecht, N.; Weis, A.; Bein, T. Formation of stable 2D methylammonium antimony iodide phase for lead-free perovskite-like solar cells. *Journal of Physics: Energy* **2020**, *2* (2), 24007.
(22) McCall, K. M.; Stoumpos, C. C.; Kostina, S. S.; Kanatzidis, M. G.; Wessels, B. W. Strong Electron–Phonon Coupling and Self-Trapped Excitons in the Defect Halide Perovskites A 3 M 2 I 9 (A = Cs, Rb; M = Bi, Sb). *Chem. Mater.* **2017**, *29* (9), 4129–4145. DOI: 10.1021/acs.chemmater.7b01184.
(23) McCall, K. M.; Stoumpos, C. C.; Kontsevoi, O. Y.; Alexander, G. C. B.; Wessels, B. W.; Kanatzidis, M. G. From 0D Cs 3 Bi 2 I 9 to 2D Cs 3 Bi 2 I 6 Cl 3 : Dimensional Expansion Induces a Direct Band Gap but Enhances Electron–Phonon Coupling. *Chem. Mater.* **2019**, *31* (7), 2644–2650. DOI: 10.1021/acs.chemmater.9b00636.
(24) Giovilli, G.; Albini, B.; Grisci, V.; Bonomi, S.; Moroni, M.; Mosconi, E.; Kaiser, W.; Angelis, F. de; Galinetto, P.; Malavasi, L. Band gap tuning through cation and halide alloying in mechanochemically synthesized Cs 3 (Sb 1− x Bi x) 2 Br 9 and Cs 3 Sb 2 (I 1− x Br x) 9 solid solutions. *J. Mater. Chem. C* **2023.** DOI: 10.1039/D3TC01492D.
(25) Harikesh, P. C.; Mulmudi, H. K.; Ghosh, B.; Goh, T. W.; Teng, Y. T.; Thirumal, K.; Lockrey, M.; Weber, K.; Koh, T. M.; Li, S.; Mhaisalkar, S.; Mathews, N. Rb as an Alternative Cation for Templating Inorganic Lead-Free Perovskites for Solution Processed Photovoltaics. *Chem. Mater.* **2016**, *28* (20), 7496–7504. DOI: 10.1021/acs.chemmater.6b03310.
(26) Mitzi, D. B. Templating and structural engineering in organic–inorganic perovskites. *J. Chem. Soc., Dalton Trans.* **2001**, *0* (1), 1–12. DOI: 10.1039/B007070J.
(27) Turkevych, I.; Kazaoui, S.; Ito, E.; Urano, T.; Yamada, K.; Tomiyasu, H.; Yamagishi, H.; Kondo, M.; Aramaki, S. Photovoltaic Rudorffites: Lead-Free Silver Bismuth Halides Alternative to Hybrid Lead Halide Perovskites. *ChemSusChem* **2017**, *10* (19), 3754–3759. DOI: 10.1002/cssc.201700980. Published Online: Jul. 6, 2017.

(28) Lu, C.; Zhang, J.; Sun, H.; Hou, D.; Gan, X.; Shang, M.; Li, Y.; Hu, Z.; Zhu, Y.; Han, L. Inorganic and Lead-Free AgBiI 4 Rudorffite for Stable Solar Cell Applications. *ACS Appl. Energy Mater.* **2018**, *1* (9), 4485–4492. DOI: 10.1021/acsaem.8b01202.
(29) Pai, N.; Lu, J.; Gengenbach, T. R.; Seeber, A.; Chesman, A. S. R.; Jiang, L.; Senevirathna, D. C.; Andrews, P. C.; Bach, U.; Cheng, Y.-B.; Simonov, A. N. Silver Bismuth Sulfoiodide Solar Cells: Tuning Optoelectronic Properties by Sulfide Modification for Enhanced Photovoltaic Performance. *Adv. Energy Mater.* **2019**, *9* (5), 1803396. DOI: 10.1002/aenm.201803396.
(30) Tie, S.; Zhao, W.; Huang, W.; Xin, D.; Zhang, M.; Yang, Z.; Long, J.; Chen, Q.; Zheng, X.; Zhu, J.; Zhang, W.-H. Efficient X-ray Attenuation Lead-Free AgBi2I7 Halide Rudorffite Alternative for Sensitive and Stable X-ray Detection. *The journal of physical chemistry letters* **2020**, *11* (19), 7939–7945. DOI: 10.1021/acs.jpclett.0c02343. Published Online: Sep. 9, 2020.
(31) Ye, H.; Sun, B.; Wang, Z.; Liu, Z.; Zhang, X.; Tan, X.; Shi, T.; Tang, Z.; Liao, G. High performance flexible memristors based on a lead free AgBiI 4 perovskite with an ultralow operating voltage. *J. Mater. Chem. C* **2020**, *8* (40), 14155–14163. DOI: 10.1039/D0TC03287E.
(32) Grandhi, G. K.; Al-Anesi, B.; Pasanen, H.; Ali-Löytty, H.; Lahtonen, K.; Granroth, S.; Christian, N.; Matuhina, A.; Liu, M.; Berdin, A.; Pecunia, V.; Vivo, P. Enhancing the Microstructure of Perovskite-Inspired Cu-Ag-Bi-I Absorber for Efficient Indoor Photovoltaics. *Small (Weinheim an der Bergstrasse, Germany)* **2022**, *18* (35), e2203768. DOI: 10.1002/smll.202203768. Published Online: Jul. 9, 2022.
(33) Al-Anesi, B.; Grandhi, G. K.; Pecoraro, A.; Sugathan, V.; Viswanath, N.; Ali-Löytty, H.; Liu, M.; Ruoko, T.-P.; Lahtonen, K.; Manna, D.; Toikkonen, S.; Muñoz-García, A. B.; Pavone, M.; Vivo, P. *Antimony-bismuth alloying: the key to a major boost in the efficiency of lead-free perovskite-inspired indoor photovoltaics*, 2023. DOI: 10.26434/chemrxiv-2023-nb5jj.
(34) Nishikubo, R.; Kanda, H.; García-Benito, I.; Molina-Ontoria, A.; Pozzi, G.; Asiri, A. M.; Nazeeruddin, M. K.; Saeki, A. Optoelectronic and Energy Level Exploration of Bismuth and Antimony-Based Materials for Lead-Free Solar Cells. *Chem. Mater.* **2020**, *32* (15), 6416–6424. DOI: 10.1021/acs.chemmater.0c01503.
(35) Gray, M. B.; McClure, E. T.; Holzapfel, N. P.; Evaristo, F. P.; Windl, W.; Woodward, P. M. Exploring the AgSb1−xBixI4 phase diagram: Thermochromism in layered CdCl2-type semiconductors. *Journal of Solid State Chemistry* **2021**, *297*, 121997. DOI: 10.1016/j.jssc.2021.121997.
(36) Ferro, D.; Nappi, B.; Piacente, V. Vapour pressure of antimony triiodide. *The Journal of Chemical Thermodynamics* **1979**, *11* (2), 193–201.
(37) Nishikubo, R.; Kanda, H.; Garcia-Benito, I.; Molina-Ontoria, A.; Pozzi, G.; Asiri, A. M.; Nazeeruddin, M. K.; Saeki, A. Optoelectronic and energy level exploration of bismuth and antimony-based materials for lead-free solar cells. *Chemistry of Materials* **2020**, *32* (15), 6416–6424.
(38) Oldag, T.; Aussieker, T.; Keller, H.-L.; Preitschaft, C.; Pfitzner, A. Solvothermale Synthese und Bestimmung der Kristallstrukturen von AgBiI4 und Ag3BiI6. *Z. anorg. allg. Chem.* **2005**, *631* (4), 677–682. DOI: 10.1002/zaac.200400508.
(39) Chakraborty, A.; Pai, N.; Zhao, J.; Tuttle, B. R.; Simonov, A. N.; Pecunia, V. Rudorffites and Beyond: Perovskite-Inspired Silver/Copper Pnictohalides for Next-Generation Environmentally Friendly Photovoltaics and Optoelectronics. *Advanced Functional Materials* **2022**, *32* (36), 2203300.
(40) Gray, M. B.; McClure, E. T.; Holzapfel, N. P.; Evaristo, F. P.; Windl, W.; Woodward, P. M. Exploring the AgSb1−xBixI4 phase diagram: Thermochromism in layered CdCl2-type semiconductors. *Journal of Solid State Chemistry* **2021**, *297*, 121997. DOI: 10.1016/j.jssc.2021.121997.
(41) Luo, H.; Wu, J.; Liu, X.; Yang, Y.; Liu, Q.; Zhang, M.; Yuan, P.; Sun, W.; Lan, Z.; Lin, J. Thiourea interfacial modification for highly efficient planar perovskite solar cells. *ACS Applied Energy Materials* **2018**, *1* (12), 6700–6706.
(42) Patil, J. V.; Mali, S. S.; Hong, C. K. A thiourea additive-based quadruple cation lead halide perovskite with an ultra-large grain size for efficient perovskite solar cells. *Nanoscale* **2019**, *11* (45), 21824–21833.

(43) Wang, S.; Ma, Z.; Liu, B.; Wu, W.; Zhu, Y.; Ma, R.; Wang, C. High-performance perovskite solar cells with large grain-size obtained by using the Lewis acid-base adduct of thiourea. *Solar Rrl* **2018**, *2* (6), 1800034.
(44) Yang, Y.; Liu, C.; Cai, M.; Liao, Y.; Ding, Y.; Ma, S.; Liu, X.; Guli, M.; Dai, S.; Nazeeruddin, M. K. Dimension-controlled growth of antimony-based perovskite-like halides for lead-free and semitransparent photovoltaics. *ACS applied materials & interfaces* **2020**, *12* (14), 17062–17069.
(45) Lu, C.; Zhang, J.; Sun, H.; Hou, D.; Gan, X.; Shang, M.; Li, Y.; Hu, Z.; Zhu, Y.; Han, L. Inorganic and Lead-Free AgBiI4 Rudorffite for Stable Solar Cell Applications. *ACS Applied Energy Materials* **2018**, *1* (9), 4485–4492. DOI: 10.1021/acsaem.8b01202.
(46) Sansom, H. C.; Whitehead, G. F. S.; Dyer, M. S.; Zanella, M.; Manning, T. D.; Pitcher, M. J.; Whittles, T. J.; Dhanak, V. R.; Alaria, J.; Claridge, J. B. AgBiI4 as a lead-free solar absorber with potential application in photovoltaics. *Chemistry of Materials* **2017**, *29* (4), 1538–1549.
(47) Xiao, Z.; Meng, W.; Mitzi, D. B.; Yan, Y. Crystal structure of AgBi2I7 thin films. *The journal of physical chemistry letters* **2016**, *7* (19), 3903–3907.
(48) Mashadieva, L. F.; Aliev, Z. S.; Shevelkov, A. V.; Babanly, M. B. Experimental investigation of the Ag–Bi–I ternary system and thermodynamic properties of the ternary phases. *Journal of Alloys and Compounds* **2013**, *551*, 512–520. DOI: 10.1016/j.jallcom.2012.11.033.
(49) Kulkarni, A.; Ünlü, F.; Pant, N.; Kaur, J.; Bohr, C.; Jena, A. K.; Öz, S.; Yanagida, M.; Shirai, Y.; Ikegami, M.; Miyano, K.; Tachibana, Y.; Chakraborty, S.; Mathur, S.; Miyasaka, T. Concerted Ion Migration and Diffusion-Induced Degradation in Lead-Free Ag 3 BiI 6 Rudorffite Solar Cells under Ambient Conditions. *Solar Rrl* **2021**, *5* (8), 2100077. DOI: 10.1002/solr.202100077.
(50) Koedtruad, A.; Goto, M.; Amano Patino, M.; Tan, Z.; Guo, H.; Nakamura, T.; Handa, T.; Chen, W.-T.; Chuang, Y.-C.; Sheu, H.-S.; Saito, T.; Kan, D.; Kanemitsu, Y.; Wakamiya, A.; Shimakawa, Y. Structure–property relations in Ag–Bi–I compounds: potential Pb-free absorbers in solar cells. *J. Mater. Chem. A* **2019**, *7* (10), 5583–5588. DOI: 10.1039/C8TA11227D.
(51) Merker, A.; Morgenroth, M.; Scholz, M.; Lenzer, T.; Oum, K. Critical Evaluation of the Photovoltaic Performance of (AgI) x (BiI 3) y Thin Films from the Viewpoint of Ultrafast Spectroscopy and Photocurrent Experiments. *J. Phys. Chem. C* **2023**, *127* (3), 1487–1498. DOI: 10.1021/acs.jpcc.2c06147.
(52) Li, Z.; Kavanagh, S. R.; Napari, M.; Palgrave, R. G.; Abdi-Jalebi, M.; Andaji-Garmaroudi, Z.; Davies, D. W.; Laitinen, M.; Julin, J.; Isaacs, M. A.; Friend, R. H.; Scanlon, D. O.; Walsh, A.; Hoye, R. L. Z. Bandgap lowering in mixed alloys of Cs 2 Ag(Sb x Bi 1−x)Br 6 double perovskite thin films. *J. Mater. Chem. A* **2020**, *8* (41), 21780–21788. DOI: 10.1039/D0TA07145E.
(53) Buizza, L. R. V.; Sansom, H. C.; Wright, A. D.; Ulatowski, A. M.; Johnston, M. B.; Snaith, H. J.; Herz, L. M. Interplay of Structure, Charge-Carrier Localization and Dynamics in Copper-Silver-Bismuth-Halide Semiconductors. *Advanced Functional Materials* **2022**, *32* (6), 2108392. DOI: 10.1002/adfm.202108392.
(54) Hooijer, R.; Weis, A.; Biewald, A.; Sirtl, M. T.; Malburg, J.; Holfeuer, R.; Thamm, S.; Amin, A. A. Y.; Righetto, M.; Hartschuh, A.; Herz, L. M.; Bein, T. Silver-Bismuth Based 2D Double Perovskites (4FPEA) 4 AgBiX 8 (X = Cl, Br, I): Highly Oriented Thin Films with Large Domain Sizes and Ultrafast Charge-Carrier Localization. *Advanced Optical Materials* **2022**, *10* (14), 2200354. DOI: 10.1002/adom.202200354.
(55) Wright, A. D.; Buizza, L. R. V.; Savill, K. J.; Longo, G.; Snaith, H. J.; Johnston, M. B.; Herz, L. M. Ultrafast Excited-State Localization in Cs2AgBiBr6 Double Perovskite. *The journal of physical chemistry letters* **2021**, *12* (13), 3352–3360. DOI: 10.1021/acs.jpclett.1c00653. Published Online: Mar. 30, 2021.
(56) Sirtl, M. T.; Armer, M.; Reb, L. K.; Hooijer, R.; Dörflinger, P.; Scheel, M. A.; Tvingstedt, K.; Rieder, P.; Glück, N.; Pandit, P.; Roth, S. V.; Müller-Buschbaum, P.; Dyakonov, V.; Bein, T. Optoelectronic Properties of Cs 2 AgBiBr 6 Thin Films: The Influence of Precursor Stoichiometry. *ACS Appl. Energy Mater.* **2020**, *3* (12), 11597–11609. DOI: 10.1021/acsaem.0c01308.
(57) Kim, Y.; Yang, Z.; Jain, A.; Voznyy, O.; Kim, G.-H.; Liu, M.; Quan, L. N.; García de Arquer, F. P.; Comin, R.; Fan, J. Z.; Sargent, E. H. Pure Cubic-Phase Hybrid Iodobismuthates AgBi2 I7 for Thin-

Film Photovoltaics. *Angewandte Chemie (International ed. in English)* **2016**, *55* (33), 9586–9590. DOI: 10.1002/anie.201603608. Published Online: Jun. 29, 2016.
(58) Zhu, H.; Erbing, A.; Wu, H.; Man, G. J.; Mukherjee, S.; Kamal, C.; Johansson, M. B.; Rensmo, H.; Odelius, M.; Johansson, E. M. J. Tuning the Bandgap in Silver Bismuth Iodide Materials by Partly Substituting Bismuth with Antimony for Improved Solar Cell Performance. *ACS Appl. Energy Mater.* **2020**, *3* (8), 7372–7382. DOI: 10.1021/acsaem.0c00712.
(59) Hsiao, K.-C.; Yu, Y.-F.; Ho, C.-M.; Jao, M.-H.; Chang, Y.-H.; Chen, S.-H.; Chang, Y.-H.; Su, W.-F.; Lee, K.-M.; Wu, M.-C. Doping engineering of carrier transporting layers for ambient-air-stable lead-free rudorffite solar cells prepared by thermal-assisted doctor blade coating. *Chemical Engineering Journal* **2023**, *451*, 138807. DOI: 10.1016/j.cej.2022.138807.
(60) Crovetto, A.; Hajijafarassar, A.; Hansen, O.; Seger, B.; Chorkendorff, I.; Vesborg, P. C. K. Parallel Evaluation of the BiI 3 , BiOI, and Ag 3 BiI 6 Layered Photoabsorbers. *Chem. Mater.* **2020**, *32* (8), 3385–3395. DOI: 10.1021/acs.chemmater.9b04925.
(61) Sansom, H. C.; Buizza, L. R. V.; Zanella, M.; Gibbon, J. T.; Pitcher, M. J.; Dyer, M. S.; Manning, T. D.; Dhanak, V. R.; Herz, L. M.; Snaith, H. J.; Claridge, J. B.; Rosseinsky, M. J. Chemical Control of the Dimensionality of the Octahedral Network of Solar Absorbers from the CuI-AgI-BiI3 Phase Space by Synthesis of 3D CuAgBiI5. *Inorganic Chemistry* **2021**, *60* (23), 18154–18167. DOI: 10.1021/acs.inorgchem.1c02773. Published Online: Nov. 9, 2021.
(62) Park, J. W.; Lim, Y.; Doh, K.-Y.; Jung, M. T.; Jeon, Y. in; Yang, I. S.; Choi, H.; Kim, J.; Lee, D.; Lee, W. in. Enhancement of the photovoltaic properties of Ag 2 BiI 5 by Cu doping. *Sustainable Energy Fuels* **2021**, *5* (5), 1439–1447. DOI: 10.1039/D0SE01563F.